Comprehensive Control of MMC-HVDC Integrated Offshore Wind Farm System Including Optimized Energy Control for Fast Frequency Support

Kangyi Sun, Hongyu Zhou, *Student Member*, *IEEE*, Wei Yao, *Senior Member*, *IEEE*, Bitao Xiao, and Jinyu Wen, *Member*, *IEEE*

***Abstract*—This paper presents a comprehensive control of modular multilevel converter-based high-voltage direct current (MMC-HVDC) integrated offshore wind farm (OWF) system, which is aimed at enhancing the fast frequency support capability. The comprehensive control consists of the active energy control (AEC), the optimized energy control (OEC), and the OWF control. The proposed OEC decouples the voltage of MMC submodule (SM) capacitor and the DC-link voltage of the MMC-HVDC. A mathematical model of the energy release process in an MMC and onshore frequency dynamics is developed, and a sinusoidal-function-based energy utilization preset curve is derived to theoretically achieve optimized frequency support, while ensuring the constrained energy usage. Upon the occurrence of a frequency event, MMC SMs may adjust their responses according to the energy utilization preset curve. The MMC then provides onshore frequency support by releasing energy. The coordination process with the OWF is also explored to further enhance the frequency support performance. Finally, case studies are conducted on the PSCAD/EMTDC platform through employing actual engineering parameters. The frequency support performance of various controls under both load increase and load decrease conditions are compared, demonstrating the effectiveness of the proposed OEC.**

***Index Terms*—Modular multilevel converter-based high-voltage direct current (MMC-HVDC), offshore wind farm (OWF), frequency support, active energy control (AEC), optimized energy control (OEC).**

Manuscript received: September 2, 2024; revised: December 23, 2024; accepted: March 28, 2025. Date of CrossCheck: March 28, 2025. Date of online publication: May 21, 2025.

This work was supported by the National Natural Science Foundation of China (No. 523B2074) and Regional Innovation and Development Joint Fund of National Natural Science Foundation of China (No. U24B2087).

K. Sun, H. Zhou (corresponding author), W. Yao, and J. Wen are with State Key Laboratory of Advanced Electromagnetic Engineering and Technology, Huazhong University of Science and Technology, Wuhan, China (e-mail: imkysun@foxmail.com; ee.henryzhou@foxmail.com; w.yao@hust.edu.cn; jinyu.wen@hust.edu.cn).

B. Xiao is with Guodian Nanjing Automation Co., Ltd., Nanjing, China (e-mail: hustxbt@163.com).

DOI: 10.35833/MPCE.2024.000975

I. Introduction

MODULAR multilevel converter-based high-voltage direct current (MMC-HVDC) is a long-distance transmission technology that is suitable for offshore wind projects, such as Borwin 1-4, Dolwin 1-6, and Helwin 1-2 in Germany and the Dogger Bank in the UK [1]-[3]. The increasing scale of offshore wind power has resulted in two main issues. First, the expansion of offshore wind farms (OWFs) reduces the proportion of traditional synchronous generators, resulting in a decrease in system inertia. Second, because the OWF is connected to the grid through a DC transmission line, a decoupling effect occurs between the offshore and onshore frequencies. This prevents OWFs from responding to onshore frequency fluctuations [4]. To address the issue of frequency stability degradation caused by the gradually increasing scale of OWF in the future, it is essential to investigate appropriate controls.

Additional controls are required to enable the MMC-HVDC integrated OWF to provide active frequency support to the onshore grid. There are two main types of such additional controls, which are implemented in the wind turbine (WT) and DC systems. The mechanism of additional control designed for an OWF is to utilize the kinetic energy of the rotor in the WT to smooth out power imbalances caused by sudden load changes [5]-[7]. Another additional control is the load-shedding control, where the WT does not initially operate at the maximum power point tracking (MPPT) position, thereby retaining a certain amount of energy. The energy margin can be used to provide frequency support when sudden load increases [8]. However, the output power of the WT is inherently stochastic, and its available energy is limited at low wind speeds. Therefore, there is an urgent need to explore other devices with potential frequency support.

Several studies have investigated the use of DC capacitor energy storage in voltage source converter-based high-voltage direct current (VSC-HVDC) transmission systems for frequency support. The capacitors can be charged or discharged to absorb or release energy, enabling short-term power regulation. Various strategies for frequency support using VSC-HVDC are proposed in [9]-[11]. Reference [9] derives the inertia coefficients that emulate the inertia of the synchronous generator using capacitive energy. Reference [10] provides a detailed explanation of implementing additional control based on frequency deviation through a DC-link voltage reference. Reference [11] discusses the application of frequency-voltage droop control to transmit the frequency signal to the system on the opposite side of the DC transmission line, which enables frequency support between two asynchronous grids. References [12] and [13] further explore the issue of increasing the energy utilization margin of the voltage source converter (VSC) capacitor. The effects of the setting of the droop factor on the frequency support results are studied in [12]. For a specific frequency deviation, a larger capacitor can be used to limit the DC-link voltage variation and to provide the required simulated inertia time constant [13].

The feasibility of utilizing submodule (SM) energy in MMC-HVDC system for frequency support is investigated in [14]-[24]. Reference [14] proposes that a portion of the bridge-arm capacitors in the converter station can be repurposed as energy storage units. Simulations demonstrate that converting only 4% of the bridge-arm capacitors can provide support power equivalent to approximately 10% of the system rated power. The factors that influence the equivalent inertia coefficient of the SM energy are explored in [15]. Reference [16] proposes a multimode active inertia support strategy for MMC-HVDC systems considering the constraint of DC-link voltage fluctuations. However, the coupling between the DC-link voltage and voltage of MMC SM capacitor limits the amount of available SM energy. Since the voltage of MMC SM capacitor and DC-link voltage can be decoupled, the utilization of SM energy becomes more flexible [17]-[19]. The inertia coefficient of a SM based on the maximum allowable frequency deviation in the grid is designed in [20]. A method for adjusting droop and inertia coefficients is proposed in [21]. In [22], the OWFs and MMC-HVDC systems are treated as an integrated unit, efficiently increasing the equivalent capacitance of the MMC-HVDC. Although [22] achieves the efficient coordination between MMC-HVDC and OWFs, it does not address the optimized utilization of energy stored in the MMC SMs.

Researchers propose new ideas for the optimization of energy utilization. An optimized method for WTs to maximize the frequency nadir is proposed in [23]. The optimized frequency trajectory is determined by decoupling the WT response and the frequency dynamics. Subsequently, the optimal additional power reference for the WT is derived from the average system frequency (ASF) model. However, the ASF model relies on extensive grid parameter measurements for controller design, leading to high communication costs and potential errors. An energy release preset curve for converter stations is proposed in [24]. However, the design of this curve lacks a solid theoretical foundation. To achieve more effective frequency support, it is crucial to investigate controls that maximize the energy utilization of the MMC. Although the aforementioned studies have employed the capacitive energy of MMC for frequency support, there is no existing control focusing on maximizing the energy utilization of the MMC. Moreover, there is a lack of theoretical analysis regarding the optimized principles for energy utilization of the MMC.

This study develops a mathematical model of the energy release process in an MMC and onshore frequency dynamics. An optimized energy control (OEC) is proposed to support grid frequency in response to sudden onshore load changes. The proposed OEC enables more efficient energy utilization of the MMC compared with existing controls. The effectiveness of the proposed OEC is demonstrated through theoretical analysis and simulation verification.

The main contributions of this paper are outlined as follows.

1) The boundaries of finite-energy storage for achieving optimized frequency support are analyzed from an energy perspective. It is found that the optimized frequency support requires two key principles. First, the energy is fully utilized within the margin. Second, the frequency nadir and energy margin are reached simultaneously. This derivation provides a theoretical foundation for the further development of the proposed OEC.

2) A sinusoidal-function-based energy utilization preset curve for the MMC is proposed based on active energy control (AEC). The relationship between the available MMC energy and the rate of change in frequency (RoCoF) is established.

3) A comprehensive control of MMC-HVDC integrated OWF system is designed, which includes AEC, OEC, and OWF control. In addition, the proposed OEC of the MMC is coordinated with the OWF control to further improve the frequency modulation performance. The effectiveness of the proposed OEC is evaluated through simulations.

The remainder of this study is organized as follows. Section II presents the finite-energy optimized frequency support principle. Section III outlines the framework of comprehensive control of MMC-HVDC integrated OWF system. The detailed explanation of each step in Section III is provided in Section IV. Section V shows the simulation verification. Finally, conclusions are provided in Section VI.

II. Finite-energy Optimized Frequency Support Principle

The structure of the comprehensive control of MMC-HVDC integrated OWF system studied in this paper is depicted in Fig. 1. The definitions of each variable can be found in [1]. The available energy from MMCs is relatively small compared with that of the dedicated energy storage devices. Moreover, the time during which energy can support frequency regulation is limited. As a result, it is essential to explore a control that can maximize the energy utilization to achieve optimized frequency regulation performance.

A. Step-wise Inertia Control

To achieve the optimized frequency support for an MMC, we first analyze the frequency response of the MMC-HVDC integrated OWF system (which is simplified as a single-machine system) with limited energy storage.

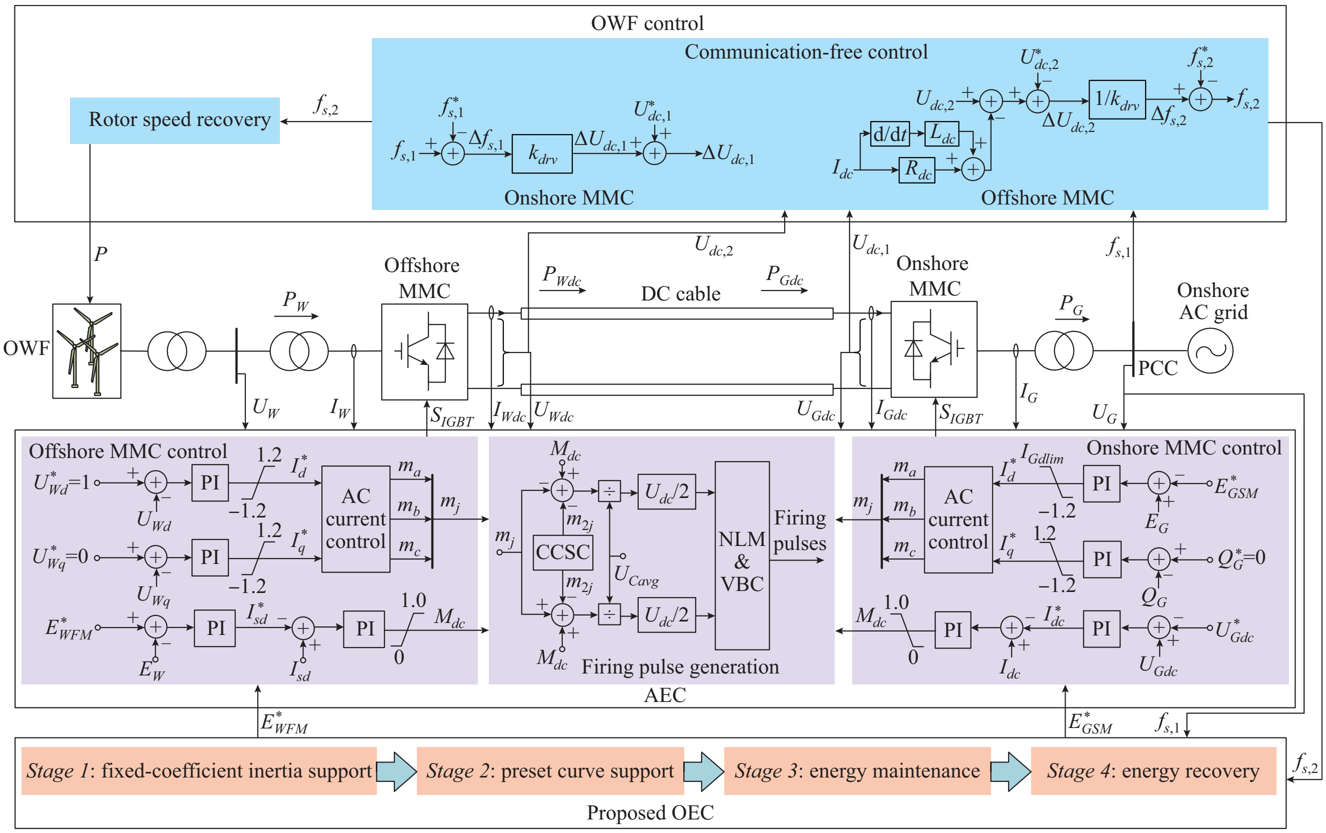

Fig. 1. Structure of comprehensive control of MMC-HVDC integrated OWF system.

Currently, additional control is commonly used to emulate the inertia response and primary frequency regulation of synchronous generators. In this subsection, the MMC applies step-wise inertia control, which effectively decouples the frequency from the energy released by the MMC.

When integrating a large-scale wind farm into the MMC-HVDC integrated OWF system, the classical system frequency response (SFR) model becomes inadequate. The wind power penetration rate ρ must be taken into account. With the introduction of ρ, the modified SFR model is proposed. The block diagram of modified SFR model for the MMC-HVDC integrated OWF system is illustrated in Fig. 2, where H is the synchronous generator inertia time constant; D is the damping factor; K_m is the mechanical power gain factor; F_H is the fraction of the total power generated by the high-pressure turbine; T_R is the reheat time constant; k_{in} is the inertia coefficient of MMCs; ΔP_{mmc} is the variation of the output power of MMCs; ΔP_L is the variation of load; ΔP_m is the variation of the output power of the generator; Δf is the variation of frequency; s is the Laplace operator; and R is the regulation factor of the governor.

Clearly, the wind power penetration rate affects the parameters H, D, and K_m. To simplify the transfer function, the equivalent parameters of H, D, and K_m are defined as:

$$H_{eq}=(1-\rho)H \tag{1}$$

$$D_{eq}=(1-\rho)D \tag{2}$$

$$K_{meq}=(1-\rho)K_m \tag{3}$$

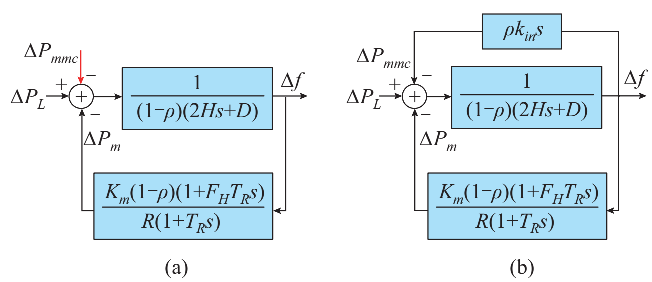

Fig. 2. Block diagram of modified SFR model for MMC-HVDC integrated OWF system. (a) Step-wise inertia control. (b) Inertia control.

where H_{eq}, D_{eq}, and K_{meq} are the equivalent parameters of H, D, and K_m, respectively.

The transfer function of the modified SFR model can be expressed as:

$$\Delta f(s)=\frac{1}{2H_{eq}s+D_{eq}}\left(\Delta P_L(s)-\Delta P_m(s)-\Delta P_{mmc}(s)\right) \tag{4}$$

$$\Delta P_m(s)=\frac{K_{meq}(1+F_H T_R s)}{R(1+T_R s)}\Delta f(s) \tag{5}$$

We assume that there is a sudden change in load, which sets ΔP_L as a step function, as shown in (6).

$$\Delta P_L(s)=\Delta P_L\frac{1}{s} \tag{6}$$

By substituting (4) and (5) into (6), the change in angular velocity $\Delta\omega$ can be obtained as:

$$\begin{cases} \Delta\omega = \dfrac{R\omega_n^2}{DR+K_m} \dfrac{(1+T_R s)(\Delta P_{mmc}-\Delta P_L)}{s(s^2+2\zeta\omega_n s+\omega_n^2)} \\ \omega_n^2 = \dfrac{D_{eq}R+K_{meq}}{2H_{eq}RT_R} \\ \zeta = \dfrac{2H_{eq}R+(D_{eq}R+K_{meq}F_H)T_R}{2(D_{eq}R+K_{meq})}\omega_n \end{cases} \tag{7}$$

where t is the time.

The inverse Laplace transform of (7) provides the frequency resolution in the time domain [25], which is given as:

$$\Delta f(t) = (\Delta P_{mmc}-\Delta P_L) r(1+\alpha e^{-\zeta\omega_n t}\sin(\omega_r t+\phi)) \tag{8}$$

$$\begin{cases} r = \dfrac{R}{DR+K_{meq}} \\ \alpha = \sqrt{\dfrac{1-2T_R\zeta\omega_n+T_R^2\omega_n^2}{1-\zeta^2}} \\ \omega_r = \omega_n\sqrt{1-\zeta^2} \\ \phi = \arctan\left(\dfrac{\omega_r T_R}{1-\zeta\omega_n T_R}\right) - \arctan\left(\dfrac{\sqrt{1-\zeta^2}}{-\zeta}\right) \end{cases} \tag{9}$$

When the energy storage device releases its energy, the frequency support terminates. Therefore, the SFR model under step-wise inertia control illustrated in Fig. 2(a) must be modified. The equivalent power disturbance of the MMC-HVDC integrated OWF system ΔP_d is shown in (10). We assume that the frequency support of the MMC starts at the beginning, and t_0 is the support termination time.

$$\Delta P_d = (\Delta P_{mmc}-\Delta P_L)h(t) - \Delta P_{mmc}h(t-t_0) \tag{10}$$

where $h(t)$ is the Heaviside-step function.

Clearly, the input variables of the MMC-HVDC integrated OWF system are not continuous. Since the modified SFR model is linear, the overall frequency response can be expressed as [26]:

$$\Delta f(t) = (\Delta P_{mmc}-\Delta P_L)h(t) r(1+\alpha e^{-\zeta\omega_n t}\sin(\omega_r t+\phi)) - \\ \Delta P_{mmc} r h(t-t_0)(1+\alpha e^{-\zeta\omega_n (t-t_0)}\sin(\omega_r (t-t_0)+\phi)) \tag{11}$$

Equation (11) in the form of a segmented function yields:

$$\Delta f(t) = \begin{cases} (\Delta P_{mmc}-\Delta P_L) r(1+\alpha e^{-\zeta\omega_n t}\sin(\omega_r t+\phi)) & t < t_0 \\ (\Delta P_{mmc}-\Delta P_L) r(1+\alpha e^{-\zeta\omega_n t}\sin(\omega_r t+\phi)) - \\ \quad \Delta P_{mmc} r(1+\alpha e^{-\zeta\omega_n (t-t_0)}\sin(\omega_r (t-t_0)+\phi)) & t \geq t_0 \end{cases} \tag{12}$$

The energy released by the MMC is related to its output power, which is given as:

$$\Delta P_{mmc} = \frac{\Delta E}{t_0} \tag{13}$$

where ΔE is the variation of the energy released by the MMC.

The modified SFR model developed above is validated through simulation. Parameters and values of the modified SFR model are listed in Table I.

With the same energy margin, Fig. 3 shows the frequency and power under different support termination time. It is worth mentioning that the frequency response illustrated in Fig. 3(b) exhibits that, different support termination time leads to varying frequency nadirs. Additionally, the frequency shows 1-2 nadirs. This is because the support termination time creates an instantaneous power deficit, resulting in a secondary frequency drop (SFD). Consequently, it is crucial to coordinate the two frequency nadirs and maximize their values.

TABLE I
PARAMETERS AND VALUES OF MODIFIED SFR MODEL

Parameter	Value
H	4.00 s
D	1.00 p.u.
K_m	0.95 p.u.
F_H	0.30 p.u.
T_R	8.00 s
R	0.05 p.u.
ρ	0.20 p.u.

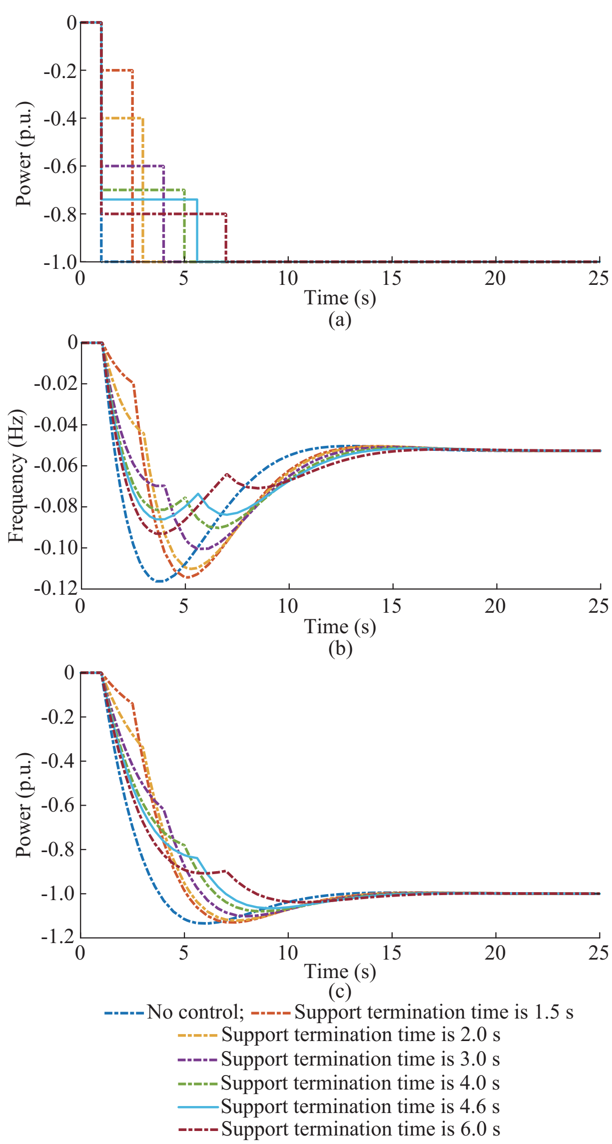

Fig. 3. Frequency and power under different support termination time. (a) Equivalent power disturbance. (b) Frequency response. (c) Output power of generator.

When the finite-energy frequency support terminates before the first frequency drop occurs, only a single frequency nadir is observed (scenario 1: one frequency nadir exists). Conversely, if the finite-energy frequency support continues beyond the first frequency drop, a second frequency nadir emerges (scenario 2: two frequency nadirs exist). Both scenarios are analyzed below.

1) Scenario 1: One Frequency Nadir Exists

Because no frequency nadir occurs during $t<t_0$, only the frequency response for $t \ge t_0$ is analyzed. The expression of $\Delta f(t)$ is given as:

$$\Delta f(t)=\left(\frac{\Delta E}{t_0}-\Delta P_L\right) r(1+\alpha \mathrm{e}^{-\zeta\omega_n t}\sin(\omega_r t+\phi))-\frac{\Delta E}{t_0} r(1+\alpha \mathrm{e}^{-\zeta\omega_n (t-t_0)}\sin(\omega_r (t-t_0)+\phi)) \tag{14}$$

Taking the derivative of (14), we can obtain that:

$$\Delta f'(t)=\left(\frac{\Delta E}{t_0}-\Delta P_L\right) r\alpha\omega_n \mathrm{e}^{-\zeta\omega_n t}\sin(\omega_r t+\phi')-\frac{\Delta E}{t_0} r\alpha\omega_n \mathrm{e}^{-\zeta\omega_n (t-t_0)}\sin(\omega_r (t-t_0)+\phi') \tag{15}$$

$$\phi'=\phi-\arctan\left(\frac{-\sqrt{1-\zeta^2}}{\zeta}\right) \tag{16}$$

Setting $\Delta f'(t)=0$, we can obtain:

$$\tan(\omega_r t+\phi')=\frac{\sin(\omega_r t+\phi')}{\cos(\omega_r t+\phi')}=X(t_0)\frac{-\dfrac{\Delta E}{t_0}\mathrm{e}^{\zeta\omega_n t_0}\sin(\omega_r t_0)}{\dfrac{\Delta E}{t_0}(1-\mathrm{e}^{\zeta\omega_n t_0}\cos(\omega_r t_0))-\Delta P_L} \tag{17}$$

where $X(t_0)$ is the a complex algebraic term dependent on time t_0.

Defining the time to reach the frequency nadir as t_{n2}, we can obtain:

$$t_{n2}=\frac{\arctan(X(t_0))-\phi'}{\omega_r} \tag{18}$$

Substituting (18) into (14), we can obtain the variation of frequency at time t_{n2}:

$$\Delta f_{n2}=-\Delta P_L r(1+\alpha \mathrm{e}^{-\zeta\omega_n t_{n2}}\sin(\omega_r t_{n2}+\phi))+\frac{\Delta E}{t_0} r\alpha(\mathrm{e}^{-\zeta\omega_n t_{n2}}\sin(\omega_r t_{n2}+\phi)-\mathrm{e}^{-\zeta\omega_n \Delta t}\sin(\omega_r \Delta t+\phi)) \tag{19}$$

$$\Delta t=t_{n2}-t_0 \tag{20}$$

Analyze the monotonicity of (19). It is known that when t_0 is limited to 0, $X(t_0)$ increases monotonically. Therefore, it can be concluded that t_{n2} also increases monotonically. Since $t_{n2}>t_0$, $\alpha \mathrm{e}^{-\zeta\omega_n \Delta t}\sin(\omega_r \Delta t+\phi)$ decreases monotonically. Also, because the stored energy of the energy storage device is low, it cannot completely eliminate the load disturbance, which means $\Delta E/t_0 << \Delta P_L$.

Therefore, it can be concluded that the lowest point of Δf_{n2} monotonically increases with t_0. This indicates that for the second frequency nadir, the longer t_0, the more effective the frequency regulation.

2) Scenario 2: Two Frequency Nadirs Exist

In this scenario, there are two frequency nadirs in frequency response, and the factors influencing these two frequency nadirs are analyzed. The time to reach the two frequency nadirs are set as t_{n1} and t_{n2}. It is worth mentioning that t_{n2} in this scenario is the same as that in (18).

When $t_0 \le t_{n1}$, by substituting t_{n1} into (12), the first frequency nadir can be derived as:

$$\Delta f_{n1}=\Delta f(t_{n1})=r\left(\frac{\Delta E}{t_0}-\Delta P_L\right)(1+\alpha \mathrm{e}^{-\zeta\omega_n t_{n1}}\sqrt{1-\zeta^2}) \tag{21}$$

$$t_{n1}=\frac{-\phi'}{\omega_r} \tag{22}$$

Since the finite-energy frequency support has not yet terminated, t_{n1} is only related to the parameters of MMC-HVDC integrated OWF system. Therefore, from (21), we know that Δf_{n1} monotonically decreases with respect to t_0.

When $t_0>t_{n1}$, the monotonicity of Δf_{n2} analyzed in scenario 1 still holds. Thus, Δf_{n2} monotonically increases with t_0.

In summary, the monotonicities of Δf_{n1} and Δf_{n2} with respect to t_0 are opposite. Therefore, there must exist a specific t_0 that makes $\Delta f_{n1}=\Delta f_{n2}$, as shown in Fig. 4. If the support termination time is $t_{0\text{opt}}$, the two frequency nadirs become equal. At this point, the frequency deviation is minimized, suggesting that the MMC-HVDC integrated OWF system achieves the best frequency support effect. This phenomenon is also illustrated in Fig. 3(c). It can be observed that when $t_0=4.6$ s, the frequency support terminates while P_m reaches its maximum value. Therefore, the essence of the frequency support is to coordinate the output power of the MMC with that of the generator.

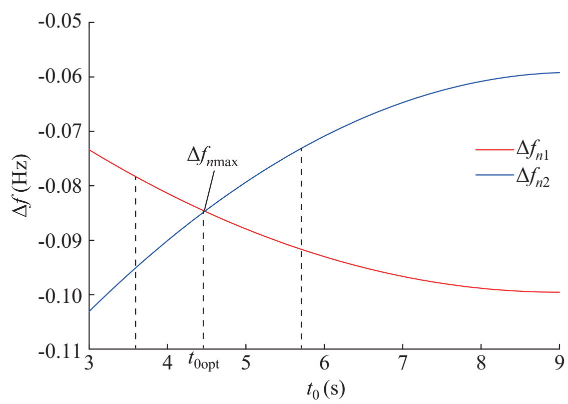

Fig. 4. Frequency nadirs according to different support termination time.

B. Inertia Control

If the energy of the MMC is released at a constant power, it is likely to cause a severe SFR. Many studies use inertia control to simulate the frequency response process of generators. Figure 2(b) illustrates the modified SFR model of the MMC-HVDC integrated OWF system under inertia control. P_{mmc} has the following relationship with frequency f.

$$P_{mmc}=\rho k_{in}\frac{\mathrm{d}f}{\mathrm{d}t} \tag{23}$$

Under the inertia control, the output power of the MMC peaks immediately following a frequency event. When the frequency reaches its nadir, RoCoF becomes 0, at which point the power output of the MMC P_{mmc} also drops to 0. In contrast to step-wise inertia control, this avoids abrupt power reduction, theoretically eliminating SFD.

Figure 5 shows the ideal illustration of frequency deviation and output power of MMC under inertia control. As illustrated in Fig. 5, if the inertia coefficient is appropriately set, the frequency of the MMC reaches its minimum when the energy is fully released. The benefit is that all the available energy can be utilized for frequency support, whereas the MMC does not diminish the support effect of the generators. Therefore, a more effective frequency support is achieved.

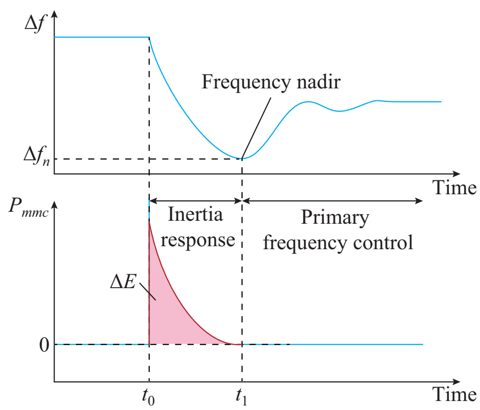

Fig. 5. Ideal illustration of frequency deviation and output power of MMC under inertia control.

Assuming an ideal inertia coefficient k_{in} that satisfies the above requirements exists and integrating both sides of (23), we can obtain that:

$$\Delta E = -\rho k_{in} \Delta P_L r (1 + \alpha e^{-\zeta \omega_n t_n} \sqrt{1-\zeta^2}) \tag{24}$$

$$\omega_n^2 = \frac{1}{2(H_{eq} + \rho k_{in}) R T_R} \tag{25}$$

$$\zeta = \frac{[2(H_{eq} + \rho k_{in}) R + F_H T_R] \omega_n}{2} \tag{26}$$

Thus, the ideal inertia coefficient k_{in} can be derived by solving (24) by using the parameters of the MMC-HVDC integrated OWF system. However, (24) is nonlinear, and the actual system is more complex than the modified SFR model previously analyzed. As a result, solving for k_{in} is challenging. Thus, the same objective can be achieved by using more simplified control, rather than the inertia control.

III. Framework of Comprehensive Control of MMC-HVDC Integrated OWF System

This section outlines the framework of the comprehensive control of the MMC-HVDC integrated OWF system. As illustrated in Fig. 1, the comprehensive control of the MMC-HVDC integrated OWF system comprises three primary control segments: AEC, the proposed OEC, and OWF control.

A. AEC

The MMC-HVDC system includes numerous energy storage components, such as capacitors and inductors [19]. During a frequency event in the onshore AC grid, the energy storage device of the flexible system can actively absorb or release energy to support the frequency response. Considering the practical projects of the MMC-HVDC integrated OWF system, half-bridge MMCs are applied in this paper. The MMC-HVDC system contains two types of capacitive energy storage device: the capacitance of the offshore or onshore MMC C_{SM} and the equivalent capacitance of DC cable line C_L. This paper focuses solely on C_{SM}.

Under the inertia control of the MMC-HVDC system, which is proposed in [17], the DC-link voltage is maintained equal to the sum of the voltage of MMC SM capacitor of the bridge arm. The voltage of MMC SM capacitor possesses a higher overvoltage margin than the DC-link voltage [27]. However, the coupling between them restricts the MMC capacitor from fully utilizing its overvoltage capability.

To overcome this issue, a method is proposed to decouple voltage of MMC SM capacitor from the DC-link voltage, thereby enhancing the flexibility of AEC [28]. A description of AEC for MMC-HVDC system is provided below.

1) Offshore MMC Control

For the offshore MMC, the rate of change in energy E_{mmc} of all its SMs is the difference between AC power and DC power, as shown in (27).

$$\frac{dE_{mmc}}{dt} = P_{ac} - P_{dc} = \frac{3}{2} U_{sd} I_{sd} - U_{dc} I_{dc} \tag{27}$$

where P_{ac} and P_{dc} are the AC power and DC power of offshore MMC, respectively; U_{sd} is the d-axis component of MMC AC-side voltage; I_{sd} is the d-axis component of MMC AC-side current; I_{dc} is the DC-link current; and U_{dc} is the DC-link voltage.

The double-closed-loop DC control can be designed as:

$$\begin{cases} I_{dc}^* = k_p (E_{WFM} - E_{WFM}^*) + k_i \int (E_{WFM} - E_{WFM}^*) dt \\ M_{dc} = k_{p,1} (I_{dc}^* - I_{dc}) + k_{i,1} \int (I_{dc}^* - I_{dc}) dt \end{cases} \tag{28}$$

where superscript * represents the reference value; E_{WFM} is the stored energy of the offshore MMC; M_{dc} is the DC modulation ratio [29]; k_p and $k_{p,1}$ are the proportional coefficients of the PI controller for I_{dc}^* and M_{dc}, respectively; and k_i and $k_{i,1}$ are the integral coefficients of the PI controller for I_{dc}^* and M_{dc}, respectively.

Furthermore, by integrating AC current control with energy control, the framework of AEC for the MMC-HVDC system can be established. With the introduction of the DC modulation ratio M_{dc} [29], the nominal DC component of the voltage of MMC SM capacitor is defined by U_{armdcn}. Taking the upper bridge arm as an example, the output voltage of the bridge arm u_{cpj} is given as:

$$u_{cpj} = \frac{U_{armdcn}}{2} (M_{dc} - m_j \cos(\omega t + \varphi_j)) \tag{29}$$

where m_j is the AC modulation ratio of phase j; ω is the angular velocity; and φ_j is the phase angle.

The current of the bridge arm i_{pj} satisfies:

$$u_{cpj}+R_0 i_{pj}+L_0\frac{\mathrm{d}i_{pj}}{\mathrm{d}t}=\frac{U_{dc}}{2}-U_{conj} \tag{30}$$

where R_0 is the equivalent arm resistance; L_0 is the equivalent arm inductance; and U_{conj} is the common-mode voltage.

Combining (29) and (30) and summing over three phases, we can obtain that:

$$R_0 I_{dc}+L_0\frac{\mathrm{d}I_{dc}}{\mathrm{d}t}=\frac{3M_{dc}}{2}U_{armdcn}-\frac{3U_{dc}}{2} \tag{31}$$

The inner-loop DC current control can be designed as:

$$M_{dc}=k_{\mathrm{p},1}(I_{dc}^*-I_{dc})+k_{\mathrm{i},1}\int(I_{dc}^*-I_{dc})\mathrm{d}t \tag{32}$$

By combining (31) and (32), a double-closed-loop DC control is formed.

2) Onshore MMC Control

The DC-link voltage and energy controls are designed as:

$$\begin{cases}I_{dc}^*=k_{\mathrm{p},2}(U_{dc}^*-U_{dc})+k_{\mathrm{i},2}\int(U_{dc}^*-U_{dc})\mathrm{d}t\\ I_d^*=k_{\mathrm{p},3}(E_{GSM}^*-E_{GSM})+k_{\mathrm{i},3}\int(E_{GSM}^*-E_{GSM})\mathrm{d}t\end{cases} \tag{33}$$

where E_{GSM} is the stored energy of the onshore MMC; $k_{\mathrm{p},2}$ and $k_{\mathrm{p},3}$ are the proportional coefficients of the PI controller for I_{dc}^* and I_d^*, respectively; $k_{\mathrm{i},2}$ and $k_{\mathrm{i},3}$ are the integral coefficients of the PI controller for I_{dc}^* and I_d^*, respectively; and I_d is the d-axis current.

The energy of the MMC SM capacitor can be designed as the outer-loop DC current control of the d-axis current controller, as shown in (34).

$$I_{sd}^*=k_{\mathrm{p},3}(E_W^*-E_W)+k_{\mathrm{i},3}\int(E_W^*-E_W)\mathrm{d}t \tag{34}$$

where E_W is the energy of MMC SM capacitor.

By combining (33) and (34), the AEC for the MMC-HVDC system is established.

3) AEC Capability Analysis

Active energy absorbing: the rated energy storage capacity of offshore MMC and onshore MMC, considering the capacitance of MMC SM capacitor C_{SM}, is given as:

$$E_{mmc0}=\frac{1}{2}C_{SM}U_{SM}^2\cdot 6N \tag{35}$$

where U_{SM} is the rated energy storage capacity of the MMC SM; and N is the total number of MMC SMs in the bridge arm.

Generally, to prevent over-voltage in MMC SM capacitor, the average individual SM capacitor voltage and the average total SM capacitor voltage are limited to 0.7 p.u. and 0.6 p.u., respectively. By regulating the voltage of MMC SM capacitor and releasing the stored energy, the MMC can compensate for the surplus power.

In this study, the upper voltage control limit is set as 1.5 p.u.. As a result, the additional energy that a single MMC can store is given as:

$$\Delta E_{mmc}=\frac{1}{2}C_{SM}(1.5^2-1)U_{SM}^2\cdot 6N=1.25E_{mmc0} \tag{36}$$

Active energy releasing: when a sudden load increase occurs in an AC system, the energy of the MMC can be actively released using the AEC to provide short-term frequency support.

To further reduce the minimum voltage of the MMC SM capacitor and enhance the energy margin, third-harmonic injection is introduced. According to [24], the relationship between the rated voltage of the MMC SM capacitor, the average voltage of the MMC SM capacitor, and the DC-link voltage is given by:

$$\begin{cases}U_{Cavgpu}=\dfrac{U_{Cavg}}{U_{CN}}\geq\dfrac{1}{2}\left(U_{dcpu}+\dfrac{\sqrt{3}}{2}M_{ac}\right)=U_{C\min}\\ U_{dcpu}\geq\dfrac{\sqrt{3}}{2}M_{ac}\end{cases} \tag{37}$$

where U_{Cavg} is the average voltage of MMC SM capacitor; U_{Cavgpu} is the per-unit value of U_{Cavg}; U_{CN} is the rated voltage of the MMC SM capacitor; U_{dcpu} is the per-unit value of U_{dc}; M_{ac} is the AC modulation ratio; and $U_{C\min}$ is the minimum value of the voltage of MMC SM capacitor.

According to (37), $U_{C\min}$ is determined by both M_{ac} and U_{dcpu}. In this paper, U_{dcpu} is set to be 1 p.u. and M_{ac} is typically chosen to be 0.85. Thus, $U_{C\min}$ is calculated as:

$$U_{C\min}=\frac{1}{2}\left(1+0.85\times\frac{\sqrt{3}}{2}\right)\approx 0.868\ \text{p.u.} \tag{38}$$

Thus, the energy that can be released by a single MMC during a short period is given as:

$$\Delta E_{mmc}=\frac{1}{2}C_{SM}(1-0.868^2)U_{SM}^2\cdot 6N=0.25E_{mmc0} \tag{39}$$

An energy margin is reserved to avoid instability, and its expression is given as:

$$\Delta E_{mmc}=0.2E_{mmc0} \tag{40}$$

B. Proposed OEC

As illustrated in Fig. 1, the process of the proposed OEC includes four stages: fixed-coefficient inertia support (stage 1), preset curve support (stage 2), energy maintenance (stage 3), and energy recovery (stage 4). The process of the proposed OEC enables the MMC to respond quickly to onshore frequency changes.

1) Fixed-coefficient Inertia Support

The purpose of stage 1 is to provide support to the onshore frequency before the maximum value of the RoCoF is reached. Because the maximum RoCoF value cannot be measured immediately during a frequency event due to measurement delays, stage 2 becomes unavailable at that moment. As a result, stage 1 employs fixed-coefficient inertia support.

2) Preset Curve Support

When the MMC senses the maximum value of RoCoF, i.e., $RoCoF_m$, it moves into stage 2. The purpose of stage 2 is to maximize the energy utilization of the MMC for optimized frequency support. The analysis in Section II demonstrates that two key principles must be met to achieve the optimized frequency support: ① the energy support must last until the frequency reaches its nadir, and ② the available energy should be used as much as possible within the energy margin. To achieve these principles, the relationship between the variation in MMC energy (which corresponds to the energy of the MMC SM capacitor) and the onshore RoCoF is established. Based on the principles proposed above, a sinusoidal-function-based energy utilization preset curve is constructed, which differs from the frequency-regulation control typically used in most studies.

3) Energy Maintenance

When the MMC energy reaches its limit, the energy level is maintained for a certain period to ensure the frequency stability.

4) Energy Recovery

Once the energy maintenance stage is completed, the MMC energy should be restored after a certain period to prepare for the next frequency event. It is important to ensure that the energy recovery moment is not too close to the moment of the frequency nadir to avoid causing a significant SFD.

C. OWF Control

In this study, the OWF control is designed to work in coordination with the MMC for the joint support of the onshore grid frequency. The OWF is equipped with conventional droop control and inertia control. When a communication-free control is employed, the transmission of the frequency signal from the onshore AC grid to the offshore MMC introduces a significant time delay [30]. Several studies explore OWFs under communication-free control [31]. In [32], a DC line carrier communication method is implemented to transmit the frequency signal over the DC-link voltage, reducing the transmission time. The DC line carrier communication method allows both the OWF and offshore MMC to sense the frequency, enabling cooperative frequency support between the MMC-HVDC system and OWF.

IV. Specific Process of Proposed OEC and OWF Control

A. Specific Process of Proposed OEC

With the establishment of the principles for the frequency support of MMC, the enhanced support can be achieved through inertia response emulation [33]. This subsection outlines the specific process of proposed OEC for onshore MMC control and offshore MMC control.

1) Onshore MMC Control

As stated earlier, two principles must be met to achieve the optimized frequency support. The energy margin is determined by the limit of the voltage of MMC SM capacitor. Clearly, the support of the MMC involves the process of RoCoF from $RoCoF_m$ to 0. It is evident that establishing the relationship between $RoCoF$ and ΔE can satisfy the principles, which can be expressed as:

$$\Delta E=\begin{cases}0 & RoCoF=RoCoF_m\\ \Delta E_{\max} & RoCoF=0\end{cases} \tag{41}$$

where $\Delta E_{\max}$ is the maximum value of ΔE.

It is known that the energy release process can simulate inertia control. From (14) and (24), it can be observed that the energy released by the MMC under the assumption of conventional control in [17] can be expressed as:

$$\Delta E(t)=k_{in}(\Delta P_{mmc}-\Delta P_L)r(1+\alpha e^{-\xi\omega_n t}\sin(\omega_r t+\phi)) \tag{42}$$

The calculation of $RoCoF(t)$ is given as:

$$RoCoF(t)=\frac{\alpha\omega_n r(\Delta P_{mmc}-\Delta P_L)}{DR+K_m}e^{-\zeta\omega_n t}\sin(\omega_r t+\phi') \tag{43}$$

Because the typical value of $\zeta\omega_n$ is small, and only the first oscillation range is considered, (42) and (43) can be simplified as:

$$\Delta E(t)=C_1+C_2\sin(\omega_r t+\phi) \tag{44}$$

$$RoCoF(t)=C_3\cos(\omega_r t+\phi') \tag{45}$$

where C_1, C_2, and C_3 are the unknown constants.

To establish the relationship of (44) and (45), we note that both equations are trigonometrically related to t. Therefore, we assume that the following relationship exists.

$$\Delta E(t)=A\sin(B\cdot RoCoF(t))=A\sin(BC_3\cos(\omega_r t+\phi')) \tag{46}$$

where A and B are the amplitude coefficient and frequency scaling factor, respectively.

The Maclaurin expansions in (46) in the range $(0,\pi)$ reveal that the result approximates the form of the cosine function. This indicates that using (46) allows the frequency response to closely resemble the inertia response. Assume that $\Delta E(t)$ can be described as:

$$\Delta E(t)=k_1+k_2\sin(k_3\cdot RoCoF(t)+\phi) \tag{47}$$

where k_1, k_2, and k_3 are the unknown constants.

Based on the two principles, the start and the end of the energy utilization preset curve can be determined as:

$$\begin{cases}\Delta E(t_{nadir})=\Delta E_{\max}\\ \Delta E(RoCoF_m)=0\end{cases} \tag{48}$$

where t_{nadir} is the time instant when ΔE reaches its minimum value.

By combining (47) and (48), a specific expression for the energy utilization preset curve is derived, as shown in Fig. 6.

$$\Delta E(RoCoF)=\Delta E_{\max}\cos\left(\frac{\pi}{2}\frac{RoCoF}{RoCoF_m}\right) \tag{49}$$

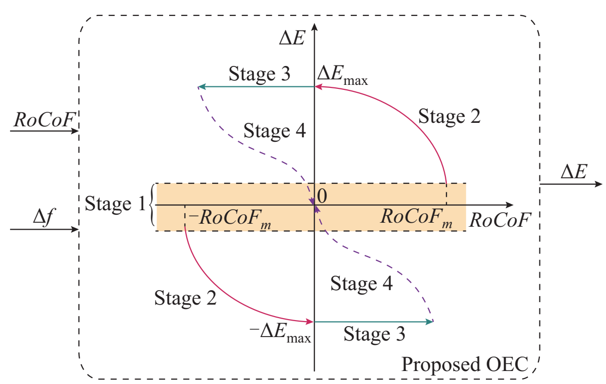

Fig. 6. Illustration of proposed OEC.

RoCoF detection requires a first-order inertia loop to prevent relay misbehavior. This introduces a delay of approximately 200-500 ms during RoCoF detection [34]. Therefore, it is not feasible to measure $RoCoF_m$ at the instant of the frequency event. To enhance the applicability of the RoCoF, the proposed OEC is designed.

1) Stage 1: fixed-coefficient inertia support

When a frequency event occurs, a signal is triggered when the frequency exceeds the limit value. The limit value is set as ±0.02 Hz [31], [35], [36]. At this point, the frequency support control of the MMC begins with fixed-coefficient inertia support. The proposed OEC cannot be utilized until $RoCoF_m$ is measured. Therefore, a conventional inertia support is applied at this stage. The fixed coefficient k_{fix} is set as:

$$k_{fix}=\begin{cases} -\dfrac{\Delta E_{\max}}{\Delta f_{\max}} & \Delta f<0 \\ \dfrac{\Delta E_{\max}}{\Delta f_{\max}} & \Delta f\geq 0 \end{cases} \tag{50}$$

where $\Delta f_{\max}$ is the maximum value of Δf.

Consider the example of a sudden increase in load. $f_{\min}$ corresponding to $\Delta f_{\max}$ is the lower frequency limit for the frequency support control by the MMC. This implies that $f_{\min}$ is the support frequency limit corresponding to the full energy released by the MMC, making full use of the energy in the MMC. $f_{\min}$ is set to be the lowest frequency allowed by the grid, thereby setting $k_{fix}=0.2/0.1=2$.

The energy used by the MMC SMs in stage 1 $\Delta E_{\max,1}$ is given as:

$$\Delta E_{\max,1}=k_{fix}\Delta f_{\max} \tag{51}$$

2) Stage 2: preset curve support

Once $RoCoF_m$ is measured, a energy utilization preset curve can be used to support the frequency. However, the energy of the MMC SM is partially released in stage 1. Therefore, it is important to calculate the amount of energy that can be used in stage 2 $\Delta E_{\max,2}$, which is given as:

$$\Delta E_{\max,2}=\Delta E_{\max}-\Delta E_{\max,1} \tag{52}$$

Substituting $\Delta E_{\max,2}$ into (49), we can perform the frequency support using preset curve support. As the RoCoF changes, the MMC automatically adjusts the amount of energy used to achieve the optimized frequency support.

3) Stage 3: energy maintenance

When the available energy in the MMC is released to the limit, it is maintained at that point for a certain period. During this time, the frequency slowly begins to rise back up. Energy is not restored immediately after the support under the proposed OEC, as preventing SFD near the nadir is important. This helps avoid further reduction in the frequency at the nadir.

4) Stage 4: energy recovery

Considering that the voltage of MMC SM capacitor must not operate at a non-rated value for an extended period, an energy recovery strategy is designed. Based on the typical timescale, the frequency recovers to a near-steady state within 10 s after the event. The energy recovery strategy is expressed as:

$$\Delta E=k_{re}(\Delta E_{\max,1}+\Delta E_{\max,2}) \tag{53}$$

The energy recovery factor k_{re} is:

$$k_{re}=\begin{cases} 1 & t<t_{sp,2}+10\text{ s} \\ -\dfrac{t-t_{sp,2}-15}{5} & t_{sp,2}+10\text{ s}\leq t\leq t_{sp,2}+15\text{ s} \\ 0 & t>t_{sp,2}+15\text{ s} \end{cases} \tag{54}$$

where $t_{sp,2}$ is the time when stage 2 ends.

Overall, the proposed OEC of the MMC changes as the frequency changes, as illustrated in Fig. 7, where $t_{sp,1}$ is the time when stage 1 ends; and t_{re} is the time when stage 4 ends.

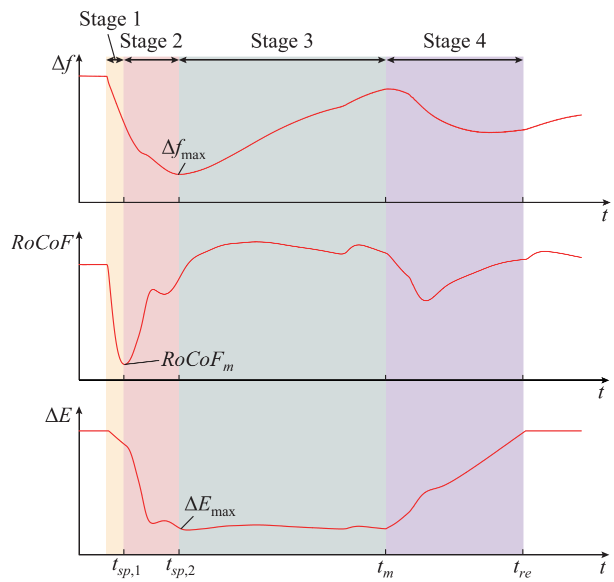

Fig. 7. Illustration of Δf, $RoCoF$, and ΔE with proposed OEC.

2) Offshore MMC Control

The energy utilization of the offshore MMC is the same as that of the onshore MMC. However, due to the decoupling effect of the DC transmission line, the offshore MMC cannot respond to frequency changes in the system immediately at the onset of a frequency event. To enable an instantaneous response from the offshore MMC, we implement a communication-free control that encodes an onshore frequency-variation signal into the DC-link voltage. The communication-free control for onshore and offshore MMCs is illustrated in Fig. 8, where subscripts 1 and 2 represent the onshore and offshore MMCs, respectively; ΔU_{dc} is the deviation of U_{dc}; k_{drv} is the droop response coefficient; L_{dc} and R_{dc} are the DC inductance and resistance, respectively; and Δf_s is the variation of frequency of MMC.

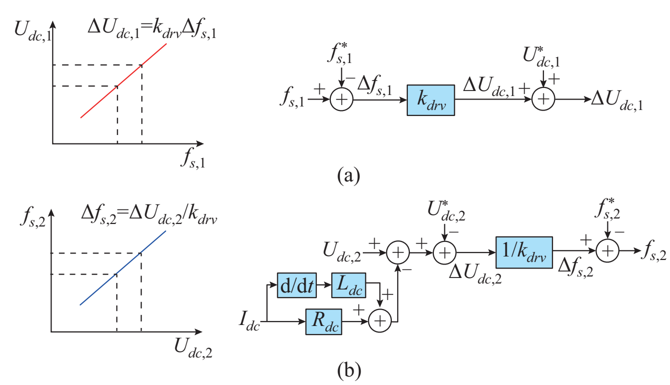

Fig. 8. Communication-free control for onshore and offshore MMCs. (a) Onshore MMC. (b) Offshore MMC.

$U_{dc,1}$-$f_{s,1}$ droop control is implemented using an onshore MMC. When the onshore frequency decreases, the onshore

DC-link voltage also decreases. According to Kirchhoff's law, the offshore DC-link voltage also decreases. The offshore MMC then uses $U_{dc,2}$-$f_{s,2}$ droop control to minimize the reference frequency of the offshore grid. The DC-link voltage drop is accounted for by obtaining the manufacturing data R_{dc} and L_{dc}. The droop coefficient should be appropriately set to ensure the accuracy of the frequency signal sent to the offshore MMC. To further enhance the accuracy of communication-free control, [31] proposes an offshore communication-free DC-link voltage estimator. This estimator uses the offshore DC-link voltage to estimate the onshore DC-link voltage for frequency support, thereby minimizing the influence of distortion.

B. Specific Process of OWF Control

An OWF employs both conventional inertia control and droop control. The rotor speed recovers within 10 s after the occurrence of frequency events. The OWF frequency is detected using the communication-free control. The limit value for OWF control is set as ±0.02 Hz.

The flow chart of the proposed OEC and the OWF control is illustrated in Fig. 9.

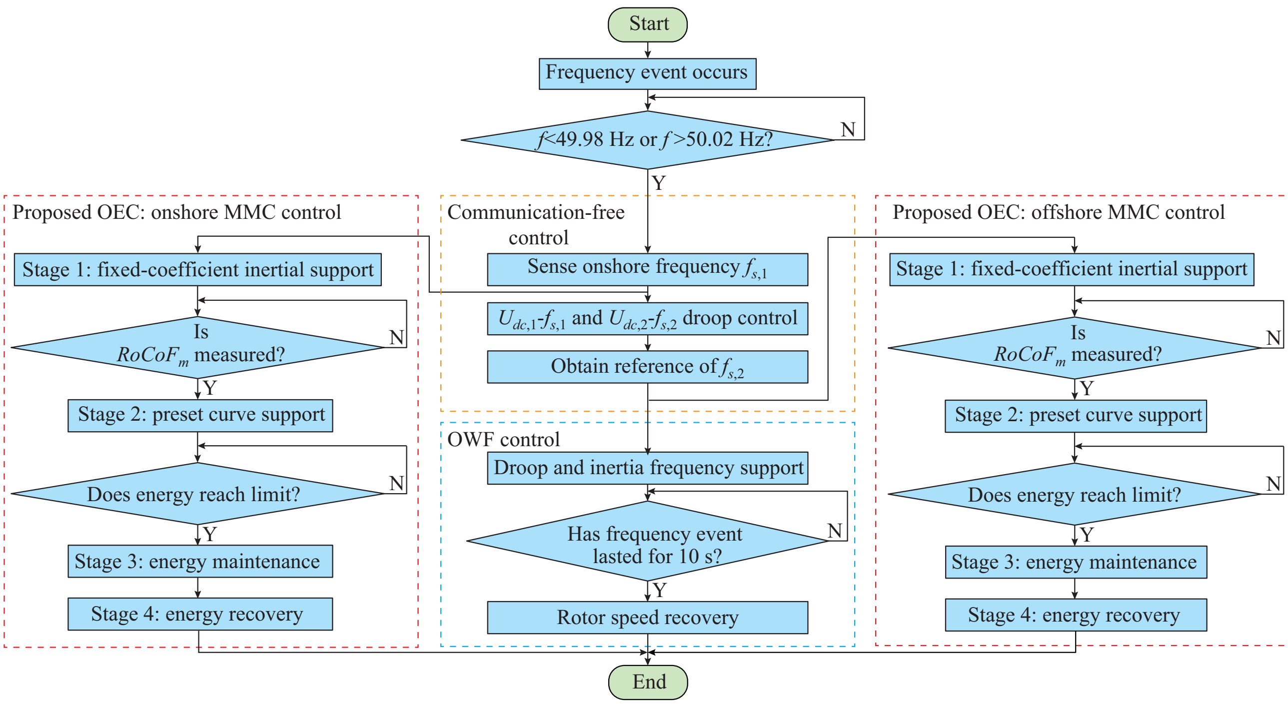

Fig. 9. Flow chart of proposed OEC and OWF control.

V. Simulation Verification

To verify the effectiveness of the comprehensive control of the MMC-HVDC integrated OWF system, the PSCAD/EMTDC platform is used to model the MMC-HVDC integrated OWF system. The onshore AC grid is represented by a synchronous generator. The transmission line is modeled using a π-section equivalent circuit. The rated capability of the onshore AC grid is 1500 MW, while the OWF power transmitted to the onshore AC grid is 1200 MW. Detailed parameters are provided in Supplementary Material A Table SAI. In this section, five kinds of control for MMC and OWF are implemented, and the frequency support effects under these controls are compared. The descriptions of different controls are provided in Table II.

A. Load Increase Event

1) 90 MW Load Increase Event

This part sets a 90 MW load increase event occurring at 30 s on the onshore MMC. The frequency responses under various kinds of control are provided in Fig. 10. The frequency under OWF control + proposed OEC is higher than those of the other kinds of control, suggesting that the proposed OEC enhances the frequency support effect. The performance of the OWF control + inertia control [20] is better than that of the OWF control, demonstrating that the energy released by the MMC compensates for the instantaneous onshore power shortage. The performance of OWF control + OEU2 [24] exceeds that of OWF control + inertia control [20], implying that the control of establishing an energy utilization preset curve allows for better utilization of the frequency support capacity of MMC. This highlights that this study further enhances the shape of the energy utilization preset curve, which further increases the frequency nadir.

Simulation results (90 MW load increase event) are illustrated in Fig. 11. The MMC samples the frequency information in real time at defined intervals. When $RoCoF_m$ is measured, $RoCoF$ is collected and input to the OEC controller to build the energy utilization preset curve. Following the 90 MW load increase event, stage 1 is triggered. Stage 2 is activated when $RoCoF_m$ is measured. The sum of the energy of the two stages can reach the upper limit of the energy released by MMC of 0.2 p.u..

TABLE II
DESCRIPTIONS OF DIFFERENT CONTROLS

Control	Description
No control	Without any frequency control
OWF control	OWF control including droop control and inertia control
OWF control + inertia control [20]	OWF control and MMC SM inertia control
OWF control + OEU2 [24]	OWF control and MMC optimized energy utilization control (quadratic correlation between ΔE and $RoCoF$) [24]
OWF control + proposed OEC	OWF control and proposed OEC (sinusoidal correlation between ΔE and $RoCoF$)

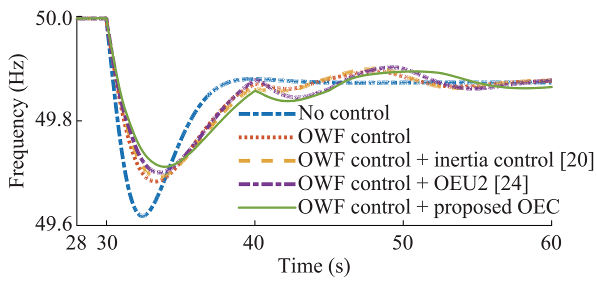

Fig. 10. Frequency responses under various kinds of control (90 MW load increase event).

Figure 12 presents the energy utilization of the onshore MMC under three controls: OWF control + inertia control [20], OWF control + OEU2 [24], and OWF control + proposed OEC. The OWF control + inertia control [20] cannot adjust the inertia coefficient adaptively, resulting in incomplete energy release, and a less pronounced frequency regulation effect.

Apparently, energy is released exactly at the same time as the frequency reaches its nadir under OWF control + proposed OEC. The DC-link voltage, which conveys the onshore frequency information, is depicted in Fig. 13.

2) 300 MW Load Increase Event

This part simulates a 300 MW load increase event occurring at 30 s. The corresponding simulation results are presented in Fig. 14(a). It is evident that the frequency nadir of OWF control + proposed OEC is higher than that observed with the other kinds of control. The effectiveness of OWF control + proposed OEC under large load disturbances is verified. The OWF control + inertia control [20] lacks the ability to adaptively adjust the inertia coefficient, resulting in early termination of energy release. As established in theoretical analysis, such premature interruption reduces the effectiveness of frequency support. This suggests that the proposed OEC delivers superior frequency support across various load increase events.

B. 450 MW Load Decrease Event

A 450 MW load decrease event is simulated onshore at 30 s. The simulation results are presented in Fig. 14(b). The OWF control + proposed OEC maintains the highest frequency nadir, demonstrating that the proposed OEC provides the most effective support effect.

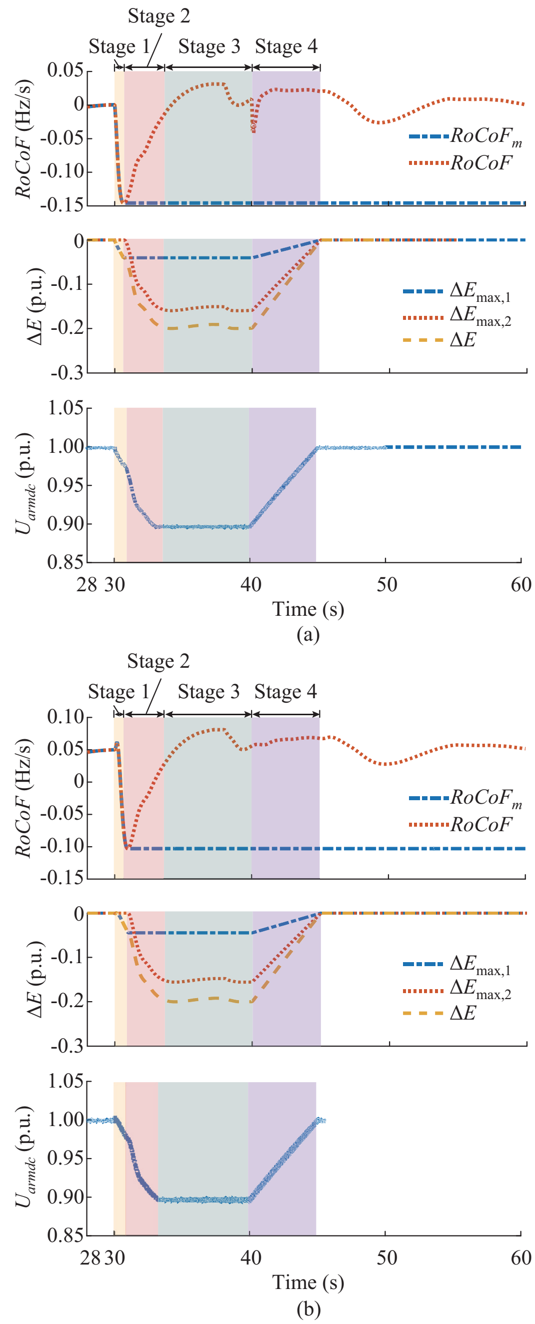

Fig. 11. Simulation results (90 MW load increase event). (a) Onshore MMC. (b) Offshore MMC.

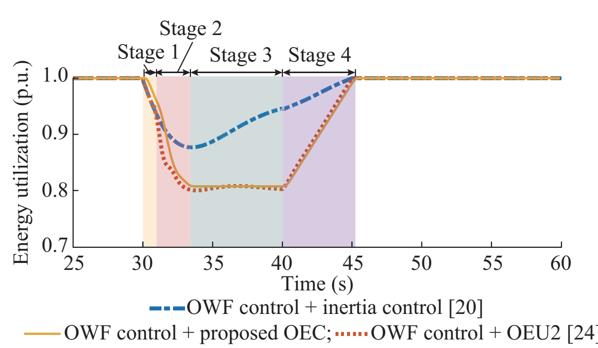

Fig. 12. Energy utilization of onshore MMC under various kinds of control (90 MW load increase event).

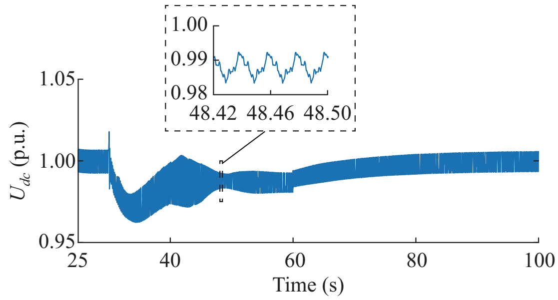

Fig. 13. Illustration of U_{dc} (90 MW load increase event).

According to Fig. 14 (b), as soon as $RoCoF_m$ is measured, it is placed in the controller to construct the energy utilization preset curve. After the load decrease event, stage 1 is entered, and stage 2 is triggered when $RoCoF_m$ is measured. The sum of the two stages can reach an upper limit of energy absorption of 1.25 p.u.. As presented in Fig. 14(b), the OWF control + inertia control [20] could not adjust the inertia coefficient adaptively, leading to an inability to absorb energy up to the upper limit. As a result, the frequency modulation effect is not as noticeable.

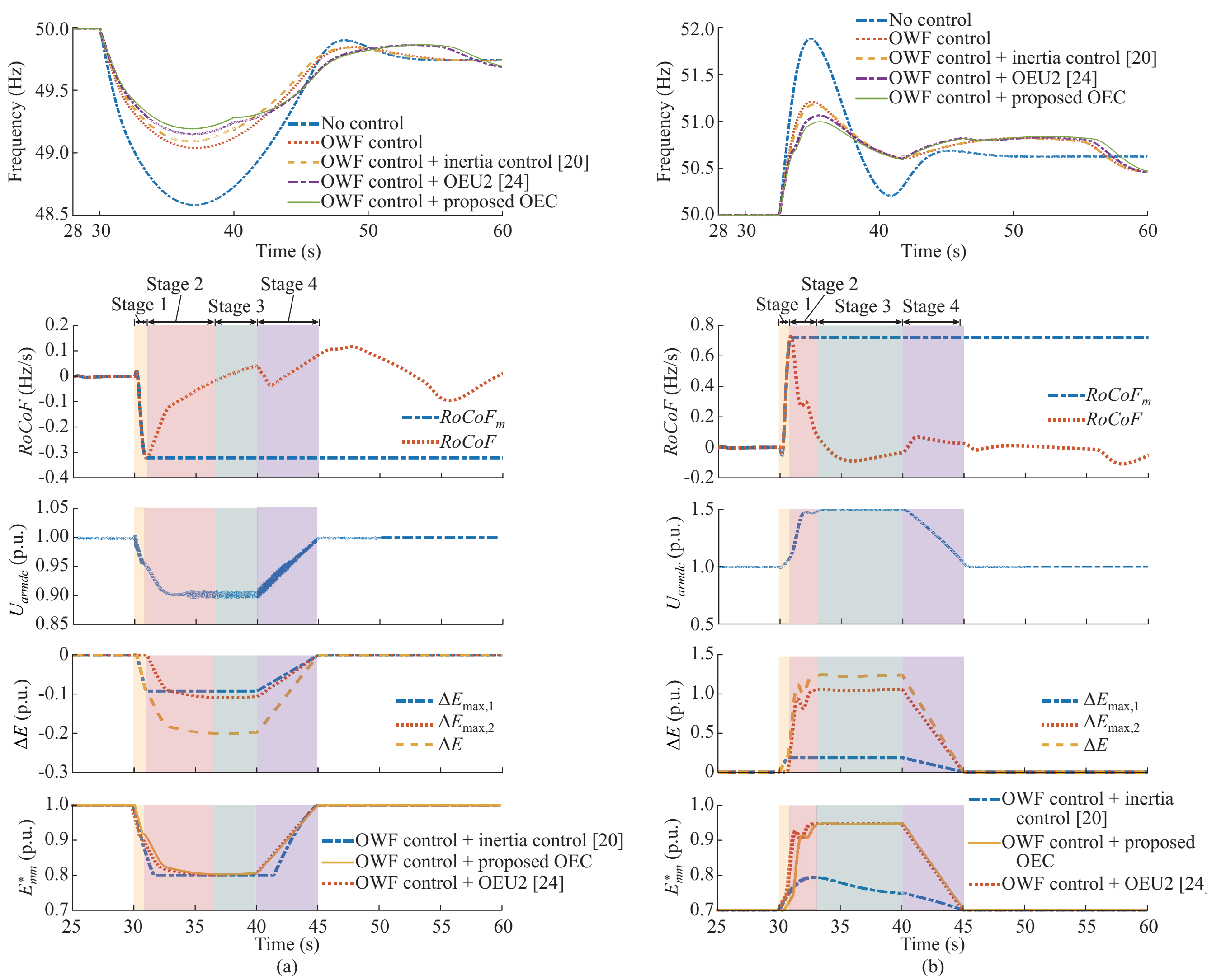

Fig. 14. Simulation results when frequency events occur. (a) 300 MW load increase event. (b) 450 MW load decrease event.

Figure 15 presents the frequency nadirs under different various kinds of events and controls. With a higher energy margin, the downward frequency support capability of the MMC is proven significantly more effective than its upward frequency support. Therefore, when a small sudden load decrease event occurs, activating only the frequency-support control of the MMC ensures both safety and stability. In this scenario, the offshore WTs operates at the MPPT point.

VI. Conclusion

This study analyzes the principle of optimized frequency support and proposes a comprehensive control of the MMC-HVDC integrated OWF system. The comprehensive control optimizes the energy utilization preset curve to maximize the frequency support capability of the MMC. Initially, the modified SFR model is utilized to analyze the finite-energy optimized frequency support principle.

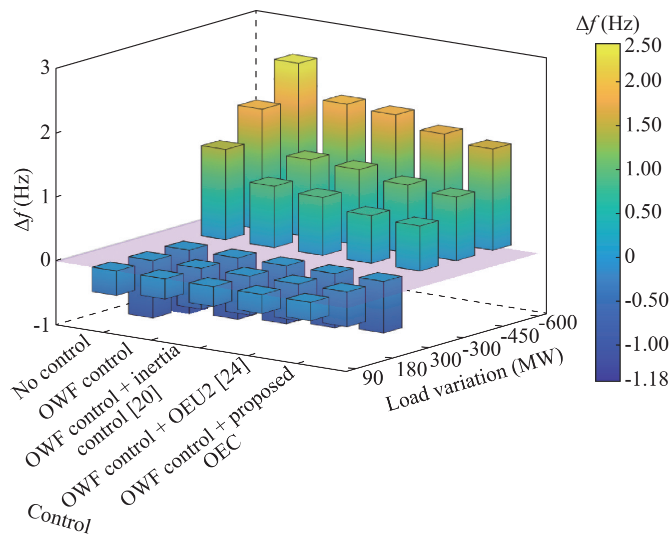

Fig. 15. Frequency nadirs under different controls and events.

It is found that when the frequency reaches the frequency nadir, the energy released by the MMC has the most significant impact on frequency support. Based on this, an OEC is proposed, where a energy utilization preset curve is designed using a sinusoidal function.

Additionally, the procedures for frequency support by the MMC in collaboration with the OWF are outlined. Case study demonstrates that the proposed OEC provides the best frequency support effect compared with the other kinds of control. The maximum frequency deviation is significantly reduced.

The proposed OEC is poised for wider application in the future. MMC offers greater energy storage in the MMC SMs, suggesting better frequency support potential. However, the energy released by the MMCs must be restricted to avoid frequency changes. Moreover, coordinating all the stations within the DC grid must be taken into account.

REFERENCES

[1] H. Zhou, W. Yao, K. Sun *et al*., "Enhancing fault ride-through and voltage support capability for MMC-HVDC integrated offshore wind farms based on multi-mode matching," *IEEE Transactions on Sustainable Energy*, vol. 15, no. 2, pp. 1256-1268, Apr. 2024.

[2] H. Zhou, W. Yao, K. Sun *et al*., "A multi-level coordinated DC overcurrent suppression scheme for symmetrical bipolar MMC-HVDC integrated offshore wind farms," *International Journal of Electrical Power & Energy Systems*, vol. 147, p. 108880, May 2023.

[3] H. Zhou, W. Yao, K. Sun *et al*., "Two-level suppressing controller of offshore DC overvoltage using zero-sequence voltage and GFL-GFM switching," *IEEE Transactions on Power Delivery*, vol. 38, no. 6, pp. 3991-4003, Dec. 2023.

[4] H. Liu and C. Liu, "Frequency regulation of VSC-MTDC system with offshore wind farms," *Journal of Modern Power Systems and Clean Energy*, vol. 12, no. 1, pp. 275-286, Jan. 2024.

[5] J. Morren, S. Haan, W. Kling *et al*., "Wind turbines emulating inertia and supporting primary frequency control," *IEEE Transactions on Power Systems*, vol. 21, no. 1, pp. 433-434, Feb. 2006.

[6] H. Zhao, H. Zhou, W. Yao *et al*., "Dynamic analysis of uniformity and difference for grid-following and grid-forming voltage source converters using phasor and topological homology methods," *Journal of Modern Power Systems and Clean Energy*, vol. 13, no. 1, pp. 3-14, Jan. 2025.

[7] M. Hwang, E. Muljadi, J. Park *et al*., "Dynamic droop-based inertial control of a doubly-fed induction generator," *IEEE Transactions on Sustainable Energy*, vol. 7, no. 3, pp. 924-933, Jul. 2016.

[8] S. Baros and M. Ilić, "Distributed torque control of deloaded wind DFIGs for wind farm power output regulation," *IEEE Transactions on Power Systems*, vol. 32, no. 6, pp. 4590-4599, Nov. 2017.

[9] J. Zhu, C. Booth, G. Adam *et al*., "Inertia emulation control strategy for VSC-HVDC transmission systems," *IEEE Transactions on Power Systems*, vol. 28, no. 2, pp. 1277-1287, May 2013.

[10] H. Liu and Z. Chen, "Contribution of VSC-HVDC to frequency regulation of power systems with offshore wind generation," *IEEE Transactions on Energy Conversion*, vol. 30, no. 3, pp. 918-926, Sept. 2015.

[11] J. Zhu, X. Wang, J. Zhao *et al*., "Inertia emulation and fast frequency-droop control strategy of a point-to-point VSC-HVDC transmission system for asynchronous grid interconnection," *IEEE Transactions on Power Electronics*, vol. 37, no. 6, pp. 6530-6543, Jun. 2022.

[12] J. Lee, S. Jeong, H. Kim *et al*., "Analytical approach for fast frequency response control of VSC HVDC," *IEEE Access*, vol. 9, pp. 91303-91313, Jun. 2021.

[13] J. Zhu, J. Guerrero, W. Hung *et al*., "Generic inertia emulation controller for multi-terminal voltage-source-converter high voltage direct current systems," *IET Renewable Power Generation*, vol. 8, no. 7, pp. 740-748, Sept. 2014.

[14] P. Judge and T. Green, "Modular multilevel converter with partially rated integrated energy storage suitable for frequency support and ancillary service provision," *IEEE Transactions on Power Delivery*, vol. 34, no. 1, pp. 208-219, Feb. 2019.

[15] S. Yang, J. Fang, Y. Tang *et al*., "Modular multilevel converter synthetic inertia-based frequency support for medium-voltage microgrids," *IEEE Transactions on Industrial Electronics*, vol. 66, no. 11, pp. 8992-9002, Nov. 2019.

[16] Z. Liu, X. Lv, F. Wu *et al*., "Multi-mode active inertia support strategy for MMC-HVDC systems considering the constraint of DC voltage fluctuations," *IEEE Transactions on Power Delivery*, vol. 38, no. 4, pp. 2767-2781, Aug. 2023.

[17] H. Saad, X. Guillaud, J. Mahseredjian *et al*., "MMC capacitor voltage decoupling and balancing controls," *IEEE Transactions on Power Delivery*, vol. 30, no. 2, pp. 704-712, Apr. 2015.

[18] H. Zhou, W. Yao, M. Zhou *et al*., "Active energy control for enhancing AC fault ride-through capability of MMC-HVDC connected with offshore wind farms," *IEEE Transactions on Power Systems*, vol. 38, no. 3, pp. 2705-2718, May 2023.

[19] H. Zhou, W. Yao, K. Sun *et al*., "Dynamic reactive current optimization based onshore AC fault ride-through strategy for MMC-HVDC integrated offshore wind farms," *IEEE Transactions on Sustainable Energy*, vol. 15, no. 2, pp. 735-746, Apr. 2024.

[20] H. Kim, J. Kang, J. W. Shim *et al*., "Exploiting redundant energy of MMC-HVDC to enhance frequency response of low inertia AC grid," *IEEE Access*, vol. 7, pp. 138485-138494, Sept. 2019.

[21] A. Leon, "Short-term frequency regulation and inertia emulation using an MMC-based MTDC system," *IEEE Transactions on Power Systems*, vol. 33, no. 3, pp. 2854-2863, May 2018.

[22] S. Jiang, H. Wang, G. Li *et al*., "A novel coordinated control strategy for frequency regulation of MMC-HVDC connecting offshore wind farms," *IEEE Transactions on Sustainable Energy*, vol. 15, no. 2, pp. 1028-1038, Apr. 2024.

[23] Y. Zhang, Z. Hao, S. Yang *et al*., "A system-view optimal additional active power control of wind turbines for grid frequency support," *IEEE Transactions on Power Systems*, vol. 39, no. 2, pp. 4323-4335, Mar. 2024.

[24] H. Zhang, W. Xiang, Y. He *et al*., "Optimal energy utilization of MMC-HVDC system integrating offshore wind farms for onshore weak grid inertia support," *IEEE Transactions on Power Systems*, vol. 39, no. 1, pp. 1304-1318, Jan. 2024.

[25] P. Anderson and M. Mirheydar, "A low-order system frequency response model," *IEEE Transactions on Power Systems*, vol. 5, no. 3, pp. 720-729, Aug. 1990.

[26] W. Bao, L. Ding, Z. Liu *et al*., "Analytically derived fixed termination time for stepwise inertial control of wind turbines: part I: analytical derivation," *International Journal of Electrical Power & Energy Systems*, vol. 121, p. 106120, Oct. 2020.

[27] K. Shinoda, A. Benchaib, J. Dai *et al*., "Virtual capacitor control: mitigation of DC voltage fluctuations in MMC-based HVDC systems," *IEEE Transactions on Power Delivery*, vol. 33, no. 1, pp. 455-465, Feb. 2018.

[28] H. Zhou, W. Yao, K. Sun *et al*., "Characteristic investigation and overvoltage suppression of MMC-HVDC integrated offshore wind farms under onshore valve-side SPG fault," *IEEE Transactions on Power Systems*, vol. 39, no. 1, pp. 1346-1359, Jan. 2024.

[29] W. Xiang, W. Lin, L. Xu *et al*., "Enhanced independent pole control

of hybrid MMC-HVDC system," *IEEE Transactions on Power Delivery*, vol. 33, no. 2, pp. 861-872, Apr. 2018.

[30] Y. Xiong, W. Yao, Y. Yao *et al*., "Distributed cooperative control of offshore wind farms integrated via MTDC system for fast frequency support," *IEEE Transactions on Industrial Electronics*, vol. 70, no. 5, pp. 4693-4704, May 2023.

[31] Y. Xiong, W. Yao, S. Lin *et al*., "Improved communication-free coordinated control of VSC-MTDC integrated offshore wind farms for onshore system frequency support," *IEEE Transactions on Power Delivery*, vol. 40, no. 2, pp. 667-680, Apr. 2025.

[32] Z. Lu, Y. Ye, and Y. Qiao, "An adaptive frequency regulation method with grid-friendly restoration for VSC-HVDC integrated offshore wind farms," *IEEE Transactions on Power Systems*, vol. 34, no. 5, pp. 3582-3593, Sept. 2019.

[33] H. Gao, P. Zi, L. Huang *et al.*, "Optimal frequency control of grid-connected power electronic devices with energy constraints," *Automation of Electric Power Systems*, vol. 44, no. 17, pp. 9-18, Sept. 2020.

[34] P. Gupta, R. Bhatia, and D. Jain, "Active ROCOF relay for islanding detection," *IEEE Transactions on Power Delivery*, vol. 32, no. 1, pp. 420-429, Feb. 2017.

[35] K. Sun, H. Zhou, W. Yao *et al*., "Two-level distributed consensus control of multiple wind farms for fast frequency support," *IEEE Transactions on Sustainable Energy*, vol. 16, no. 1, pp. 530-545, Jan. 2025.

[36] H. Zhao, Q. Zong, H. Zhou *et al.*, "Frequency-voltage active support strategy for hybrid wind farms based on grid-following and grid-forming hierarchical subgroup control," *CSEE Journal of Power and Energy Systems*, vol. 11, no. 1, pp. 65-77, Jan. 2025.

Kangyi Sun received the B. S. degree in electrical engineering from the School of Electrical and Electronic Engineering, Huazhong University of Science and Technology, Wuhan, China, in 2022. She is currently working toward the M.S. degree in the School of Electrical and Electronic Engineering, Huazhong University of Science and Technology. Her current research interests include analysis and control of new power system.

Hongyu Zhou received the B. S. degree in electrical engineering from Southwest Jiaotong University, Chengdu, China, in 2020. He is currently working toward the Ph.D. degree in electrical engineering at Huazhong University of Science and Technology, Wuhan, China. His current research interests include power system stability analysis and control, renewable energy, high-voltage direct current (HVDC), and DC grid.

Wei Yao received the B.S. and Ph.D. degrees in electrical engineering from Huazhong University of Science and Technology (HUST), Wuhan, China, in 2004 and 2010, respectively. He was a Post-Doctoral Researcher with the Department of Power Engineering, HUST, from 2010 to 2012, and a Postdoctoral Research Associate with the Department of Electrical Engineering and Electronics, University of Liverpool, Liverpool, U. K., from 2012 to 2014. Currently, he is a Professor with the School of Electrical and Electronics Engineering, HUST. His current research interests include power system stability analysis and control, renewable energy, HVDC, DC grid, and application of artificial intelligence in smart grid.

Bitao Xiao received the B. S. and M. S. degrees in electrical engineering from Huazhong University of Science and Technology (HUST), Wuhan, China, in 2001 and 2004. Currently, he is a Professor Level Senior Engineer with Guodian Nanjing Automation Co., Ltd., Nanjing, China. His current research interests include renewable energy, HVDC, and DC grid.

Jinyu Wen received the B. S. and Ph. D. degrees in electrical engineering from Huazhong University of Science and Technology (HUST), Wuhan, China, in 1992 and 1998, respectively. He was a Visiting Student from 1996 to 1997 and Research Fellow from 2002 to 2003 all at the University of Liverpool, Liverpool, U.K., and a Senior Visiting Researcher at the University of Texas at Arlington, Arlington, USA, in 2010. From 1998 to 2002, he was a Director Engineer with XJ Electric Co. Ltd., Xuchang, China. In 2003, he joined the HUST and now is a Professor with the School of Electrical and Electronics Engineering, HUST. His current research interests include renewable energy integration, energy storage application, DC grid, and power system operation and control.